ORIGINAL PAPER

Analytical basis for the determination of the lacunar–canalicular permeability of bone using cyclic loading

M. Benalla · L. Cardoso · S. C. Cowin

Abstract An analytical model for the determination of the permeability in the lacunar–canalicular porosity of bone using cyclic loading is described in this contribution. The objective of the analysis presented is to relate the lacunar–canalicular permeability to a particular phase angle that is measurable when the bone is subjected to infinitesimal cyclic strain. The phase angle of interest is the lag angle between the applied strain and the resultant stress. Cyclic strain causes the interstitial fluid to move. This movement is essential for the viability of osteocytes and is believed to play a major role in the bone mechanotransduction mechanism. However, certain bone fluid flow properties, notably the permeability of the lacunar–canalicular porosity, are still not accurately determined. In this paper, formulas for the phase angle as a function of permeability for infinitesimal cyclic strain are presented and mathematical expressions for the storage modulus, loss modulus, and loss tangent are obtained. An accurate determination of the PLC permeability will improve our ability to understand mechanotransduction and mechanosensory mechanisms, which are fundamental to the understanding of how to treat osteoporosis, how to cope with microgravity in long-term manned space flights, and how to increase the longevity of prostheses that are implanted in bone tissue.

Keywords Poroelasticity · Osteon permeability · Phase angle · Storage modulus · Loss modulus · Loss tangent

M. Benalla · L. Cardoso · S. C. Cowin (✉)
The Department of Biomedical Engineering,
The School of Engineering of The City College
and The Graduate School of The City University of New York,
New York, NY, 10031, USA
e-mail: sccowin@gmail.com

List of symbols

$\hat{A}_r, \hat{A}_\theta, \hat{A}_z$	Three components of the 6D vector representing the Biot effective stress coefficient for PLC
r	Arbitrary radius of the osteon
r_o	Outer radius of the osteon
r_i	Inner radius of the osteon
a	Non-dimensional inner radius of the Osteon ($a = r_i/r_o$)
$\hat{\mathbf{C}}^i$	(i = m, d, u) elasticity or stiffness matrix for the matrix material, drained elastic constants and undrained elastic constants (2nd order tensor in 6D)
c	Pore fluid pressure diffusion constant in the lacunar–canalicular porosity
$\hat{\mathbf{E}}$	Strain, a vector in 6D, equivalent to the strain tensor in 3D
$\mathbf{E}$	Modulus of elasticity
f_o	Constant of integration determined in Eq. (16)
I_o, I_1	Modified Bessel functions of the first kind
i	Imaginary number ($i = \sqrt{-1}$)
K^f	Compressibility of the fluid
K^i_{Reff}	Reuss lower bound on the effective (isotropic) bulk modulus of the anisotropic elastic material ($i = m, d$)
K_o, K_1	Modified Bessel functions of the second kind
K_{rr}	Radial permeability
$\tilde{p}(r, t)$	Pore fluid pressure in the PLC
$\tilde{u}(r, t)$	Displacement vector

Greek symbols

ε_o	Strain amplitude of the cyclic applied strain
ϕ	Porosity

λ	Ratio of r/r_o (non-dimensional)
ω	Angular frequency associated with the cyclic loading
$\bar{\omega}$	Dimensionless angular frequency
μ	Viscosity of the pore fluid
ν_{ij}	Poisson's ratios ($i, j = r, \theta, z$)
σ^*	Average resultant stress due the applied cyclic strain
σ_o	Magnitude of the average resultant stress
Υ	Constant of dimension force
Λ	Solid–fluid compliance contrast coefficient
$\tilde{\zeta}(r, t)$	Variation of fluid content and
C^*	Dynamic elastic modulus
δ	Phase angle

Subscripts and superscripts

d	The drained condition of the porous solid
u	The undrained condition of the porous solid
f	The fluid component
m	The matrix material of the porous solid

1 Introduction

During the last decade, an increasing amount of evidence has supported the hypothesis that osteocytes, the bone cells in the lacunae (pores) of the lacunar–canalicular porosity (PLC), are the principal mechanosensory cells of bone (Burger et al. 1995; Cowin et al. 1991; Han et al. 2004), and that they are activated by the induced drag from fluid flowing through the PLC (Cowin et al. 1995; Fritton and Weinbaum 2009; Weinbaum et al. 1994). The movement of bone fluid from the region of the bone vasculature through the canaliculi and the lacunae of the surrounding mineralized tissue is related to the poroelastic aspect of the loaded bone (Fritton et al. 2001; Rémond et al. 2008; Wang et al. 2003) that exhibits creep, stress relaxation, and a phase or lag angle between an applied cyclic strain and the resultant stress (Buechner and Lakes 2003; Cowin 1999, 2001; Lakes 1982; Nguyen et al. 2009; Swan et al. 2003). The deformation-driven fluid movement in the bone tissue accomplishes three important tasks. First, it transports nutrients to the cells in the lacunae buried in the mineralized matrix. Second, it carries away the cell waste. Third, the deformation-driven interstitial fluid movement in the PLC exerts a force on the osteocyte process, a force that is large enough for the cell to sense, which is considered as the basic mechanotransduction mechanism in bone cells in vivo.

Key to the understanding of mechanotransduction by osteocytes is knowledge of the lacunar–canalicular network permeability. An estimate of the PLC permeability was first proposed by Zeng et al. (1994) based on an ultrastructural model of the lacunar–canalicular system, predicting PLC permeability on the order of 10^{-20} to 10^{-22} m². Subsequent, theoretical estimates were based on Biot's poroelasticity theory, including the study by Wang et al. (1999) in which the PLC of bovine bone was found in the range of 10^{-20} m², the approach by Gururaja et al. (2005) who obtained an estimate of the PLC permeability in both the radial and circumferential directions to be 10^{-22} and 10^{-19} m², respectively, and the study by Zhou et al. (2008) in mice, with a PLC permeability on the order of 10^{-22} m². Traditional permeability measurement techniques based on Darcy's technique of measuring the volume of fluid flow per unit area and per unit time across a porous layer, which is then divided by the pore pressure gradient across the layer, seem to be experimentally unfeasible. Therefore, other approaches have been developed to determine the PLC permeability. Smit et al. (2002) obtained an estimate of the PLC permeability in the order of 10^{-22} m² based on the best fit between finite element predictions and data from streaming potential measurements. Beno et al. (2006) found the PLC permeability in canine samples to vary from 10^{-19} to 10^{-22} m². The PLC permeability of human bone was estimated by Oyen (2008) to be around 10^{-24} m² using nanoindentation measurements and poroelasticity theory. Curve fitting of stress relaxation of single bovine osteons and poroelasticity theory was used by Gailani et al. (2009), finding the PLC permeability to be between 10^{-24} and 10^{-25} m². An estimate of the PLC permeability was provided by Kameo et al. (2010) based on measurements of fluorescent images taken with a laser confocal microscope in trabecular bone from a swine tibia and an anisotropic poroelastic analytical model, resulting in predictions of the PLC permeability on the order of 10^{-17} m². In their discussion, Kameo et al. (2010) described difficulties with their confocal laser scanning microscopy. Only recently, the canine PLC was measured in situ by Gardinier et al. (2010) and reported as 10^{-23} m² (Table 1).

These estimates of PLC permeability exhibit a broad variability, with values ranging from 10^{-17} to 10^{-25} m² (Table 1). Such broad range of variability may be due to the different approach/model taken to determine the PLC permeability and/or by experimental challenges associated with the measurement of small quantities as in the case of Kameo et al. (2010). Importantly, the PV and the PLC are interconnected, occupying the same three-dimensional volume of bone tissue. Thus, the pore pressure in the PLC depends upon the permeability of the PV and vice versa. In order to investigate the interaction of the pore pressure and fluid flow between the PV and the PLC, a hierarchical poroelastic model was recently developed by our group (Cowin et al. 2009). On one hand, it is difficult to measure the PV permeability without the effect of the PLC since the PLC is always contained in the tissue matrix material of samples used to measure the PV. On the other hand, the PLC permeability can be measured

Table 1 Values of the PLC permeability collected from different studies. The values are ranging from 3.32×10^{-17} m^2 to 7.00×10^{-25} m^2

Reference	Method	Permeability at the PLC
Kameo et al. (2010)	Morphology of the PLC	3.32×10^{-17} to 1.26×10^{-18} m^2
Wang et al. (1999)	Theoretical study	1.47×10^{-20} m^2
Smit et al. (2002)	Finite element analysis	2.20×10^{-22} m^2
Beno et al. (2006)	Biot theory	3.32×10^{-19} to 1.26×10^{-22} m^2
Zeng et al. (1994)	Ultrastructural model	10^{-19} to 10^{-22} m^2
Gururaja et al. (2005)	Poroelasticity model	10^{-19} to 10^{-22} m^2
Zhou et al. (2008)	FRAP	10^{-22} m^2
Gardinier et al. (2010)	Step loading experiment	2.80×10^{-23} m^2
Oyen (2008)	Nanoindentation	4.14×10^{-24} m^2
Gailani et al. (2009)	Stress relaxation	3.00×10^{-24} to 7.00×10^{-25} m^2
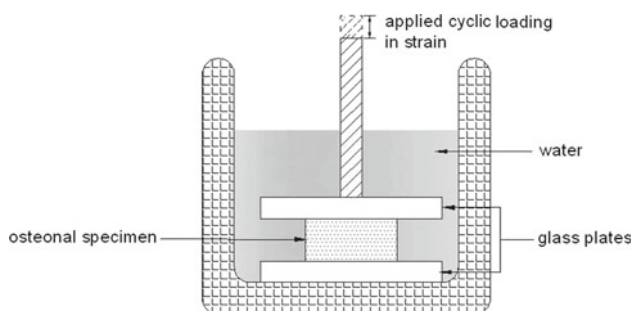
Fig. 1 Single osteon specimen immersed in water and subjected to unconfined cyclic loading. The specimen is compressed between rigid plates that are parallel, smooth, and impermeable. The interstitial fluid is forced to flow out of the PLC in the radial direction across the inner boundary of the annular region into the Haversian canal. No fluid flow is produced at the outer boundary since the cement line is assumed to be impermeable

without the effect of the PV if a sample that contains PLC only is obtained. For this purpose, the analytical solution of a saturated compressible poroelastic annular cylinder under an unconfined stress-relaxation test was developed (Gailani and Cowin 2008). Predictions made by this model were compared to experimental stress-relaxation measurements made on isolated osteons in vitro (zero blood pressure), and the curve fitting between data and experiments was used to obtain the PLC permeability without the influence of the PV (Gailani et al. 2009).

In this paper, the solution presented in Cowin et al. (2009) and the experimental approach developed in Gailani et al. (2009) are extended to the case of harmonic loading (Fig. 1). A description of the osteon's anatomy and physiology is presented in Sect. 2. A single osteon is idealized as a fully saturated porous annular cylinder subjected to an axial cyclic mechanical loading in order to determine formulas for the phase angle as a function of permeability and frequency in Sect. 3. The phase angle of interest corresponds to the difference between the applied cyclic strain and the resultant stress. Also, expressions for the storage modulus, the loss modulus,

and the loss tangent are obtained in Sect. 3. Numerical examples are presented in Sect. 4, the sensitivity of the analytical model to the variation in the model parameters is considered in Sect. 5, and a discussion of the results is in Sect. 6. The analytical model of this paper will be used as a basis of a future experimental study in which an isolated osteonal specimen will be subjected to an applied cyclic strain in order to determine the phase angle between the applied cyclic strain and the resultant stress and thus evaluate the frequency dependence of the PLC permeability experimentally.

2 The anatomy and physiology of an osteon

The osteon is a fundamental building unit of adult human long bones at the microscopic scale. The osteon geometry is roughly cylindrical with a radius of about 100–150 μm, and it contains at its center a Haversian or osteonal canal of about 40 μm radii (Fig. 2). It is composed of two phases, liquid and solid. The fluid phase is an interstitial liquid that surrounds blood vessels in the Haversian canal and fills all the pores in the PLC; it functions as an interchange path between the two porosities. The fluid movement depends upon the applied loading and the difference of pore pressure between the two chambers, the PLC and the central Haversian canal. The interchange occurs in two different directions, (i) transport of nutrients and oxygen from arterioles to the bone cells into the PLC and (ii) transfer of the cell waste from the lacunae to the venules in the central Haversian canal, part of vascular porosity (PV). The osteonal solid phase formation unit is a lamella 3–7 μm thick composed of mineralized collagen fibers oriented parallel to one another. The small regularly placed cavities observed in between lamellae are lacunae, in which osteocytes (bone cells) reside. Lacunae are connected by small canals (approximately 0.3 μm in diameter) called canaliculi. Each canaliculum contains an osteocyte cell process, and these processes are connected with each other by gap junctions. The canaliculi also join the lacunae with the
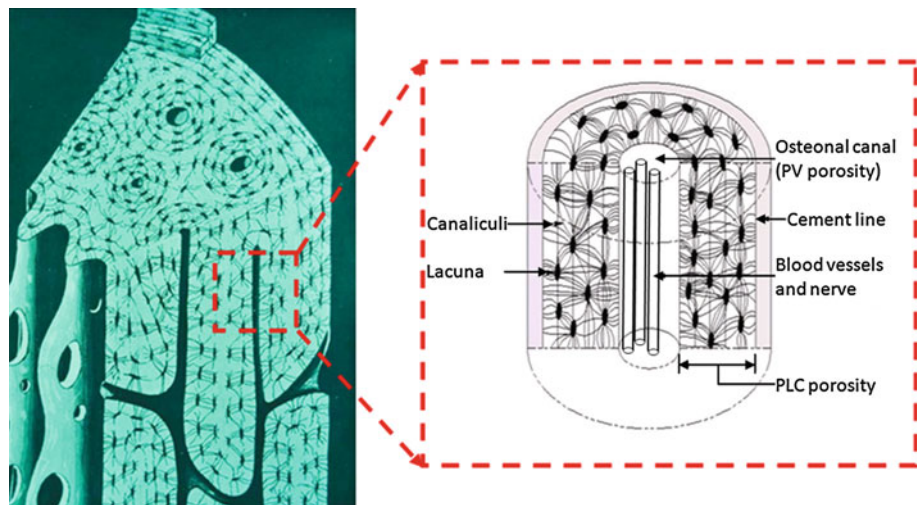
Haversian canal (Fig. 2). At the outer border of each osteon are roughly $2\,\mu$m thick cement lines comprised of a mineralized matrix (Jee 1988). The annular region of the approximately cylindrical osteon is entirely composed of the PLC and the cement line. The Haversian or osteonal canal is part of the PV and has a diameter of roughly $40\,\mu$m. The osteonal canal is considered as PV because of its size and the fact that it houses vasculature and nerves as well. Beyond the fact that the PLC houses osteocytes in the lacunae, it represents all the fluid-occupied space in an osteon. In terms of movement and velocity, the interstitial fluid behaves differently under a cyclic mechanical loading in the PLC from its behavior in the Haversian canal. The difference of the bone fluid behavior stems from the differences in geometry and the intrinsic characteristic of each domain (Fornells et al. 2007). On one hand, the Haversian canal is the large-scale porosity with roughly ten orders of magnitude greater permeability (Gardinier et al. 2010) that houses blood vessels and in which pressure pulses will decay rapidly. Any significant increase of pressure in response to mechanical loading beyond blood pressure in this porosity could collapse the vessels, which will render the bone tissue ischemic if the collapse is prolonged (Cowin et al. 2009); in other words, this means that the PV remains most of the time under a lower pressure. However, on other hand, the PLC is the porosity associated with the higher pressure compared to the PV as well as longer relaxation time for pressure pulses (Yang et al. 1999; Zhang et al. 1998). Moreover, the PLC has a much lower permeability and contains osteocytes, the bone sensory cells, with their interconnected processes. The difference of pressures created between the PLC and the PV causes the fluid movement that creates forces large enough to be sensed by osteocytes. These forces are thought to activate the molecular sensor structures that are part of the mechanosensory phenomena. The whole process allows the osteocytes to orchestrate the bone resorption and manage the bone remodeling. Therefore, one can see

how the determination of the PLC permeability represents a major key to improve the understanding of mechanotransduction phenomena.

3 Phase angle as a function of permeability

We consider a transverse segment of an isolated osteonal specimen whose annular region (PLC) between the Haversian canal and cement line is subjected to an axial cyclic loading between two smooth, parallel and impermeable plates (Figs. 1, 2). The contact between the specimen and the plates is assumed to be frictionless and the applied load is considered to be uniformly distributed on the loaded surface. The axial cyclic loading is in the form of an applied strain, $\varepsilon_o e^{i\omega t}$, where ε_o and ω are the amplitude of the cyclic strain and its angular frequency, respectively. Axial symmetry is assumed, and cylindrical coordinates are employed to represent the specimen; r is the radial coordinate, and z is the axial coordinate. The displacement in the radial direction is then denoted by $\tilde{u}(r, t)$ where t is time. These displacement components, in addition to the pore pressure field $\tilde{p}(r, t)$ and the variation in fluid content $\tilde{\zeta}(r, t)$, a dimensionless measure of the fluid mass per unit volume of the porous material, are assumed to have the following temporal dependencies when subjected to the applied axial loading $\varepsilon(t) = \varepsilon_o e^{i\omega t}$:

$$\tilde{u}(r, t) = z\varepsilon(t), \quad \tilde{p}(r, t) = p(r)e^{i\omega t}, \quad \tilde{\zeta}(r, t) = \zeta(r)e^{i\omega t}. \tag{1}$$

The differential equation governing the pore pressure field is specialized from Cowin et al. (2009, equation (5.16)), as

$$\frac{\partial^2 \tilde{p}}{\partial r^2} + \frac{1}{r}\frac{\partial \tilde{p}}{\partial r} - \frac{\mu}{K_{rr}}\left(\frac{\hat{A}_r^2}{\hat{C}_{rr}^d} + \Lambda\right)\frac{\partial \tilde{p}}{\partial t}$$
$$= i\omega\frac{\mu}{K_{rr}}\left(\hat{A}_z\varepsilon_o + \hat{A}_r f_o\right)e^{i\omega t}. \tag{2}$$

Table 2 Relationships between model parameters employed

Formulas

Constants	Transverse isotropy compressible
$\frac{1}{K_r^m}$	$\frac{1-\nu_{r\theta}^m-\nu_{rz}^m}{E_r^m}$
$\frac{1}{K_z^m}$	$\frac{1-2\nu_{rz}^m}{E_z^m}$
$\frac{1}{K_{\text{Reff}}^m}$	$\frac{2}{K_r^m}+\frac{1}{K_z^m}$
Δ_1	$1-\nu_{r\theta}^d-2\nu_{rz}^d\nu_{zr}^d$
Δ_2	$\left(1-\nu_{rz}^d\nu_{zr}^d\right)/\left(1+\nu_{r\theta}^d\right)$
Δ_3	$\left(1-2\nu_{zr}^d\right)\Delta_2/\Delta_1$
$\frac{1}{K_{\text{Reff}}^d}$	$\frac{2(1-\nu_{r\theta}^d-\nu_{rz}^d)}{E_r^d}+\frac{1-2\nu_{zr}^d}{E_z^d}$
C_{eff}^d	$\frac{1}{K_{\text{Reff}}^d}-\frac{1}{K_{\text{Reff}}^m}+\phi\left(\frac{1}{K^f}-\frac{1}{K_{\text{Reff}}^m}\right)$
Λ	$C_{eff}^d-\frac{1}{K_{\text{Reff}}^d}+\frac{2}{K_{\text{Reff}}^m}-\frac{1}{\Delta_1}\left[\frac{2E_r^d}{K_r^{m2}}+\frac{4E_r^d\nu_{zr}^d}{K_r^m K_z^m}+\frac{E_z^d\left(1-\nu_{r\theta}^d\right)}{K_z^{m2}}\right]$
J	$\left[1-\frac{E_r^d}{\Delta_1}\left(\frac{1}{K_r^m}+\frac{\nu_{zr}^d}{K_z^m}\right)\right]^2+\Lambda\frac{E_r^d\Delta_2}{\Delta_1}$
$\hat{A}_r$	$1-\frac{E_r^d}{\Delta_1}\left(\frac{1}{K_r^m}+\frac{\nu_{zr}^d}{K_z^m}\right)$
$\hat{A}_z$	$1-\frac{E_z}{\Delta_1}\left(\frac{2\nu_{rz}^d}{K_r^m}+\frac{1-\nu_{r\theta}^d}{K_z^m}\right)$
$\hat{C}_{rr}^d$	$\frac{\Delta_2}{\Delta_1}E_r^d$
$\hat{C}_{zz}^d$	$\frac{(1-\nu_{r\theta}^d)}{\Delta_1}E_z^d$
$\hat{C}_{r\theta}^d$	$\frac{1-\Delta_2}{\Delta_1}E_r^d$
$\hat{C}_{rz}^d$	$\frac{\nu_{rz}}{\Delta_1}E_z^d$
c	$\frac{K_{rr}C_{rr}^d}{\mu J}$

The notations in Eq. (2) that were not introduced above include the expressions for the radial elastic constant $\hat{C}_{rr}^d$, the radial intrinsic permeability K_{rr}, the coefficient Λ describing the contrast between the compliance of the solid tissue matrix material and the pore fluid, and the two components of the 6D vector representing the Biot effective stress coefficients $\hat{A}_z$ and $\hat{A}_r$. These symbols are introduced in the nomenclature, and their formulas are provided in Table 2. f_o is a constant of integration to be determined. Equation (2) may be written more conveniently by introducing the dimensionless driving frequency constant $\bar{\omega}$ and a constant of dimension force Υ as

$$\bar{\omega}=\frac{\omega r_o^2}{c},\quad \Upsilon=\mu\hat{A}_r c,\tag{3}$$

where c is the pore fluid diffusion constant in the PLC (Table 2), the dimensionless radius $\lambda=r/r_o$, noting that r_o corresponds to the outer radius of the osteon: Eq. (2) then takes the form

$$\frac{\partial^2\tilde{p}}{\partial\lambda^2}+\frac{1}{\lambda}\frac{\partial\tilde{p}}{\partial\lambda}-i\bar{\omega}\tilde{p}=\frac{i\bar{\omega}\Upsilon}{K_{rr}}\left(\frac{\hat{A}_z}{\hat{A}_r}\varepsilon_o+f_o\right).\tag{4}$$

The fluid flow is only in the radial direction within the annular region of the osteon (the PLC), and the solution of this ODE requires thus only two boundary conditions, (i) at $\lambda=1$,

(the outer boundary of the osteon), it is considered that there is no flow crossing the cement line, and (ii) at $\lambda=a$, (the Haversian canal wall), where a is a non-dimensional inner radius of the osteon, there is a free fluid flow between the Haversian canal and the PLC, thus

$$\frac{\partial\tilde{p}}{\partial\lambda}(1,t)=0,\quad \tilde{p}(a,t)=0.\tag{5}$$

The solution of the ODE (4) subjected to the boundary conditions (5) is

$$\tilde{p}(\lambda,t)=\left(\bar{\Pi}(\lambda,1)-1\right)\left(\frac{A_z}{A_r}\varepsilon_o+f_o\right)\frac{\Upsilon}{K_{rr}}e^{i\omega t},\tag{6}$$

where

$$\bar{\Pi}(\lambda,\alpha)=\frac{\Pi(\lambda,\alpha)}{\Pi(a,\alpha)}\quad\text{and}\quad\Pi(\lambda,\alpha)$$
$$=I_o\left(\sqrt{i\bar{\omega}}\lambda\right)K_1\left(\sqrt{i\bar{\omega}}\alpha\right)$$
$$+I_1\left(\sqrt{i\bar{\omega}}\alpha\right)K_o\left(\sqrt{i\bar{\omega}}\lambda\right).\tag{7}$$

Concerning the thought experiment associated with this model, no flow is permitted across the upper and bottom boundaries of the annular section of the osteon due to close contact with the impervious and frictionless loading plates. There also exists a free fluid exchange between the Haversian canal fluid and the fluid contacting the osteonal canal at the top and bottom of the specimen.

The non-zero stress components are given in terms of the radial displacement $\tilde{u}(r,t)$ and the pore fluid pressure by Cowin et al. (2009, equation (5.3)),

$$T_{rr}=-\hat{A}_r\tilde{p}+\hat{C}_{rr}^d\frac{\partial\tilde{u}}{\partial r}+\hat{C}_{r\theta}^d\frac{\tilde{u}}{r}+\hat{C}_{rz}^d\varepsilon_o e^{i\omega t},$$
$$T_{\theta\theta}=-\hat{A}_r\tilde{p}+\hat{C}_{r\theta}^d\frac{\partial\tilde{u}}{\partial r}+\hat{C}_{rr}^d\frac{\tilde{u}}{r}+\hat{C}_{rz}^d\varepsilon_o e^{i\omega t},$$
$$T_{zz}=-\hat{A}_z\tilde{p}+\hat{C}_{rz}^d\left(\frac{\partial\tilde{u}}{\partial r}+\frac{\tilde{u}}{r}\right)+\hat{C}_{zz}^d\varepsilon_o e^{i\omega t}.\tag{8}$$

The relationship between $\tilde{u}(r,t)$ and $\tilde{p}(r,t)$,

$$\frac{\partial\tilde{u}}{\partial r}+\frac{\tilde{u}}{r}=\frac{1}{\lambda}\frac{\partial}{\partial\lambda}(\lambda\tilde{u})=\frac{\hat{A}_r}{\hat{C}_{rr}^d}r_o\tilde{p}(\lambda,t)+r_o f_o e^{i\omega t},\tag{9}$$

is obtained by substituting the expressions for T_{rr} and $T_{\theta\theta}$ given in (8) into the stress equilibrium condition

$$\frac{\partial T_{rr}}{\partial r}+\frac{T_{rr}-T_{\theta\theta}}{r}=0,\tag{10}$$

thus, the expression for $\tilde{u}(\lambda,t)$ is given by

$$\tilde{u}(\lambda,t)=\left[\frac{1}{2}+\left(\frac{\bar{\Sigma}(\lambda,1)}{\lambda}-\frac{1}{2}\right)\right]r_o\lambda f_o e^{i\omega t}$$
$$+\frac{\lambda}{C_{rr}^d}\left(\frac{\bar{\Sigma}(\lambda,1)}{\lambda}-\frac{1}{2}\right)r_o A_z\varepsilon_o e^{i\omega t}+\frac{g_o}{\lambda}e^{i\omega t},\tag{11}$$

where

$$\Sigma(\lambda, \alpha) = \frac{1}{\sqrt{i\bar\omega}} \frac{\partial \Pi(\lambda, \alpha)}{\partial \lambda},$$

$$\int \lambda \Pi(\lambda, \alpha) d\lambda = \frac{\lambda \Sigma(\lambda, \alpha)}{\sqrt{i\bar\omega}}, \quad \bar\Sigma(\lambda, \alpha) = \frac{\Sigma(\lambda, \alpha)}{\Pi(\lambda, \alpha)},$$
(12)

and g_o is a constant of integration obtained by solving Eq. (9). The substitution of Eqs. (11) and (9) into the expression of T_{rr} in (8) yields to the desired formula for the radial stress,

$$
T_{rr} = -\hat A_r \tilde p + \left\{ \frac{\hat C_{r\theta}^d + \hat C_{rr}^d}{2} + \left[\bar\Pi(\lambda, 1) - 1 \right. \right.
$$
$$
\left. + \frac{\hat C_{r\theta}^d - \hat C_{rr}^d}{\hat C_{rr}^d} \left(\frac{\bar\Sigma(\lambda, 1)}{\lambda \sqrt{i\bar\omega}} - \frac{1}{2} \right) \right] \frac{\hat A_r \Upsilon}{K_{rr}} \right\} f_o e^{i\omega t}
$$
$$
+ \left\{ \hat C_{rz}^d + \left[\bar\Pi(\lambda, 1) - 1 + \frac{\hat C_{r\theta}^d - \hat C_{rr}^d}{\hat C_{rr}^d} \right. \right.
$$
$$
\left. \left. \times \left(\frac{\bar\Sigma(\lambda 1)}{\lambda \sqrt{i\bar\omega}} - \frac{1}{2} \right) \right] \frac{\hat A_z \Upsilon}{K_{rr}} \right\} \varepsilon_o e^{i\omega t}
$$
$$
+ \left(\hat C_{r\theta}^d - \hat C_{rr}^d \right) \frac{g_o}{r_o \lambda^2} e^{i\omega t}
$$
(13)

Because of the free fluid flow at the inner surface of the hollow cylinder, both the radial stress and the pore fluid pressure vanish. At this boundary, $\lambda = a$ and the function $\bar\Pi(\lambda, 1)$ in Eq. (7) becomes $\bar\Pi(a, 1) = 1$, thus

$$
T_{rr}(a, t) = 0 = \left\{ \frac{\hat C_{r\theta}^d + \hat C_{rr}^d}{2} \right.
$$
$$
\left. + \left[\frac{\hat C_{r\theta}^d - \hat C_{rr}^d}{\hat C_{rr}^d} \left(\frac{\bar\Sigma(a, 1)}{a \sqrt{i\bar\omega}} - \frac{1}{2} \right) \right] \frac{\hat A_r \Upsilon}{K_{rr}} \right\} f_o e^{i\omega t}
$$
$$
+ \left\{ \hat C_{rz}^d + \left[\frac{\hat C_{r\theta}^d - \hat C_{rr}^d}{\hat C_{rr}^d} \left(\frac{\bar\Sigma(a, 1)}{a \sqrt{i\bar\omega}} - \frac{1}{2} \right) \right] \frac{\hat A_z \Upsilon}{K_{rr}} \right\} \varepsilon_o e^{i\omega t}
$$
$$
+ \left(\hat C_{r\theta}^d - \hat C_{rr}^d \right) \frac{g_o}{r_o a^2} e^{i\omega t}.
$$
(14)

If we now require that the effective radial stress $T_{rr} + \hat A_r \tilde p$ vanishes at the outer surface of the osteon that corresponds to $\lambda = 1$, we obtain the following restriction:

$$
T_{rr}(1, t) + \hat A_r \tilde p = 0 = \left[\frac{\hat C_{r\theta}^d + \hat C_{rr}^d}{2} \right.
$$
$$
\left. + \left(\frac{1}{\sqrt{i\bar\omega}\Pi(a, 1)} - \frac{\hat C_{r\theta}^d + \hat C_{rr}^d}{2\hat C_{rr}^d} \right) \frac{\hat A_r \Upsilon}{K_{rr}} \right] f_o e^{i\omega t}
$$
$$
+ \left[\hat C_{rz}^d + \left(\frac{1}{\sqrt{i\bar\omega}\Pi(a, 1)} - \frac{\hat C_{r\theta}^d + \hat C_{rr}^d}{2\hat C_{rr}^d} \right) \frac{\hat A_z \Upsilon}{K_{rr}} \right] \varepsilon_o e^{i\omega t}
$$
$$
+ \left(\hat C_{r\theta}^d - \hat C_{rr}^d \right) \frac{g_o}{r_o} e^{i\omega t},
$$
(15)

where $\bar\Sigma(1, 1) = 0$ and $\bar\Pi(1, 1) = \frac{1}{\sqrt{i\bar\omega}\Pi(a,1)}$. Equations (14) and (15) permit the evaluation of the two constant of integrations f_o and g_o. As g_o is not needed to define the expression of the pore pressure (Eq. 6), only f_o is evaluated. This is accomplished by multiplying Eq. (14) by a^2 and subtracting the result from (15); thus,

$$
f_o = \frac{\left[a_1 - \hat C_{rz}^d \left(1 - a^2 \right) K_{rr} \right] \varepsilon_o}{\frac{\hat C_{r\theta}^d + \hat C_{rr}^d}{2} \left(1 - a^2 \right) K_{rr} + \left(\frac{\hat A_r - \hat A_z}{\sqrt{i\bar\omega}\Pi(a,1)} - \hat A_r \right) \Upsilon - a_1},
$$
(16)

where we have defined

$$
a_1 = \left(\frac{\hat C_{r\theta}^d - \hat C_{rr}^d}{\hat C_{rr}^d} \left(\frac{a \bar\Sigma(a, 1)}{\sqrt{i\bar\omega}} + \frac{1 - a^2}{2} \right) \right.
$$
$$
\left. - \frac{1}{\sqrt{i\bar\omega}\Pi(a, 1)} \right) \hat A_z \Upsilon.
$$
(17)

Then, by substituting Eq. (16) into (6), the expression for the pore pressure may be written in the form

$$
\tilde p(\lambda, t) = \left(\bar\Pi(\lambda, 1) - 1 \right)
$$
$$
\times \left(\frac{\hat A_z}{\hat A_r} + \frac{\left[a_1 - \hat C_{rz}^d \left(1 - a^2 \right) K_{rr} \right] \varepsilon_o}{\frac{\hat C_{r\theta}^d + \hat C_{rr}^d}{2} \left(1 - a^2 \right) K_{rr} + \left(\frac{\hat A_r - \hat A_z}{\sqrt{i\bar\omega}\Pi(a,1)} - \hat A_r \right) \Upsilon - a_1} \right)
$$
$$
\times \frac{\Upsilon}{K_{rr}} \varepsilon_o e^{i\omega t}.
$$
(18)

We are now in a position to calculate $\sigma^*(t)$, the average resultant stress due to the applied cyclic strain loading $\varepsilon(t) = \varepsilon_o e^{i\omega t}$. In this case $\sigma^*(t)$ is defined by

$$
\sigma^*(t) = \frac{2}{1 - a^2} \int_a^1 T_{zz} \lambda \, d\lambda,
$$
(19)

where $\lambda = r/r_o$ is the dimensionless radial coordinate and a is the value of λ at the inner cylindrical surface. The substitution of Eqs. (9) and (11) into the expression of T_{zz} in Eq. (8) leads to

$$
T_{zz} = - \left(\bar\Pi(\lambda, 1) - 1 \right) \left(\frac{\hat A_z}{\hat A_r} \varepsilon_o + f_o \right) \frac{\hat A_z \Upsilon}{K_{rr}} e^{i\omega t}
$$
$$
+ \hat C_{rz}^d \left[1 + \left(\bar\Pi(\lambda, 1) - 1 \right) \frac{\hat A_z \Upsilon}{\hat C_{rr}^d K_{rr}} \right] f_o e^{i\omega t}
$$
$$
+ \left(\bar\Pi(\lambda, 1) - 1 \right) \frac{\hat C_{rz}^d \hat A_z \Upsilon}{\hat C_{rr}^d K_{rr}} \varepsilon_o e^{i\omega t} + \hat C_{zz}^d \varepsilon_o e^{i\omega t};
$$
(20)

then, after replacing the expression of T_{zz} from Eq. (20) into Eq. (19) and solving the integral, the final form of $\sigma^*(t)$ becomes

$$
\sigma^*(t) = C^*(\bar\omega)\varepsilon(t),
$$
(21)

where the dynamic modulus $C^*(\bar{\omega})$ is expressed as

$$
\begin{aligned}
C^*(\bar{\omega}) = \frac{2}{1-a^2} \Bigg\{ & \left[\hat{C}^d_{rz} \frac{1-a^2}{2} - \left(\frac{\hat{A}_r}{\hat{C}^d_{rr}} \hat{C}^d_{rz} - \hat{A}_z \right) \right. \\
& \left. \times \left(\frac{a \bar{\Sigma}(a,1)}{\sqrt{i\bar{\omega}}} + \frac{1-a^2}{2} \right) \right] \\
& \times \frac{\left[a_1 - \hat{C}^d_{rz} \left(1-a^2 \right) K_{rr} \right]}{\frac{\hat{C}^d_{r\theta} + \hat{C}^d_{rr}}{2} \left(1-a^2 \right) K_{rr} + \left(\frac{\hat{A}_r - \hat{A}_z}{\sqrt{i\bar{\omega}}\Pi(a,1)} - \hat{A}_r \right) \Upsilon - a_1} \\
& + \hat{C}^d_{zz} \frac{1-a^2}{2} - \left(\frac{\hat{C}^d_{rz}}{\hat{C}^d_{rr}} - \frac{\hat{A}_z}{\hat{A}_r} \right) \left(\frac{a \bar{\Sigma}(a,1)}{\sqrt{i\bar{\omega}}} + \frac{1-a^2}{2} \right) \hat{A}_z \frac{\Upsilon}{K_{rr}} \Bigg\}.
\end{aligned}
\tag{22}
$$

In this case $C^*(\bar{\omega})$ can take the following expression

$$
C^*(\bar{\omega}) = C^d_{zz} + \frac{c_1 - c_2 K_{rr}}{c_3 K_{rr} + c_4} - \frac{c_5}{K_{rr}},
\tag{23}
$$

with c_i, (i = 1, 2, 3, 4, 5), constants, defined as

$$
\begin{aligned}
c_1 &= \left[\hat{C}^d_{rz} - \left(\frac{\hat{A}_r}{\hat{C}^d_{rr}} \hat{C}^d_{rz} - \hat{A}_z \right) \left(\frac{2a\bar{\Sigma}(a,1)}{\left(1-a^2 \right) \sqrt{i\bar{\omega}}} + 1 \right) \right] a_1, \\
c_2 &= 2\hat{C}^d_{rz} \left[\hat{C}^d_{rz} - \left(\frac{\hat{A}_r}{\hat{C}^d_{rr}} \hat{C}^d_{rz} - \hat{A}_z \right) \left(\frac{a\bar{\Sigma}(a,1)}{\sqrt{i\bar{\omega}}} + \frac{1-a^2}{2} \right) \right], \\
c_3 &= \frac{\hat{C}^d_{r\theta} + \hat{C}^d_{rr}}{2} \left(1-a^2 \right), \\
c_4 &= \left(\frac{\hat{A}_r - \hat{A}_z}{\sqrt{i\bar{\omega}}\Pi(a,1)} - \hat{A}_r \right) \Upsilon - a_1, \quad \text{and} \\
c_5 &= \left(\frac{\hat{C}^d_{rz}}{\hat{C}^d_{rr}} - \frac{\hat{A}_z}{\hat{A}_r} \right) \left(\frac{2a\bar{\Sigma}(a,1)}{\left(1-a^2 \right) \sqrt{i\bar{\omega}}} + 1 \right) \hat{A}_z \Upsilon.
\end{aligned}
\tag{24}
$$

The average resultant stress can also be written as

$$
\sigma^*(t) = \sigma_o e^{i(\omega t - \delta(\bar{\omega}))} = \sigma_o e^{-i\delta(\bar{\omega})} e^{i\omega t},
\tag{25}
$$

thus

$$
C^*(\bar{\omega}) = C_o e^{-i\delta(\bar{\omega})}, \quad C_o = \frac{\sigma_o}{\varepsilon_o},
\tag{26}
$$

where ε_o and σ_o are, respectively, the magnitudes of the applied cyclic strain and the average resultant stress in the osteon while $\delta(\bar{\omega})$ is the phase angle representing the time delay between the harmonic strain and the resultant stress. Equation (26) is an explicit form of the frequency-dependent stiffness (or dynamic modulus of elasticity) of the tissue, which is a function of the porosity and the unknown permeability as shown in Eqs. (22) and (23). The dynamic modulus $C^*(\bar{\omega})$ is thus dependent on the symmetry and compressibility conditions of the material. In this paper, we will restrict our study to the case of the transverse isotropic symmetry with compressible matrix material and a compressible fluid that corresponds to the physical properties of the osteon. In soft tissues such as cartilage, the assumption that the fluid and

Table 3 Numerical values of the model parameters employed

PLC parameter values		
Constant	Value	Unit
$E^m_r = E^m_\theta$	18.6	GPa
E^m_z	22.32	GPa
$\nu^m_{r\theta} = \nu^m_{\theta r}$	0.322	
$\nu^m_{zr} = \nu^m_{z\theta}$	0.312	
K_{rr}	10^{-22}, 10^{-23} and 10^{-24}	m^2
K_f	2.3	GPa
ϕ	[0.05, .15]	
Δ_1	0.5103	
Δ_2	0.6939	
$\hat{C}^d_{rr}$	20.63	GPa
$\hat{C}^d_{rz}$	7.479	GPa
$\hat{C}^d_{r\theta}$	7.194	GPa
$\hat{C}^d_{zz}$	18.949	GPa
$1/K^m_{Reff}$	6.23×10^{-9}	GPa^{-1}
$1/K^d_{Reff}$	8.58×10^{-9}	GPa^{-1}
Λ	4.52×10^{-9}	GPa^{-1}
$\hat{A}_r$	0.236×10^{-9}	
$\hat{A}_z$	0.216×10^{-9}	
J	0.712	
c	53.71×10^{-9}	m^2 s^{-1}

solid constituents of the poroelastic medium are both incompressible is reasonable because the bulk modulus of the tissue and its constituent fluid are about the same magnitude. For bone tissue, however, the effective bulk modulus of the poroelastic solid constituent of bone tissue is approximately six times stiffer than that of the fluid constituent (Cowin and Doty 2007). Therefore, it is apparent that the pressures in the solid and fluid phases are significantly different compared to the soft tissue situation where they are approximately the same. Thus, the constituent incompressibility assumption that is acceptable for soft tissues is inappropriate for hard tissues and if this incompressibility assumption is kept for bone tissue, large errors in the determination of bone fluid pressures will emerge.

All the parameters appearing in Eq. (22) are summarized in Table 2, and the values used for the numerical examples in Sect. 4 are expressed in Table 3. Using Euler's formula, we can write

$$
\begin{aligned}
C^*(\bar{\omega}) = C_o e^{i\delta(\bar{\omega})} &= C_o \cos[\delta(\bar{\omega})] \\
&+ iC_o \sin[\delta(\bar{\omega})] = C'(\bar{\omega}) + iC''(\bar{\omega}),
\end{aligned}
\tag{27}
$$

where $C'(\bar{\omega})$ is known as the storage modulus and $C''(\bar{\omega})$ as the loss modulus of the osteon. From the Eq. (27), the expression of the loss tangent is

$$\tan[\delta(\bar{\omega})] = \frac{C''(\bar{\omega})}{C'(\bar{\omega})} = \frac{\sin[\delta(\bar{\omega})]}{\cos[\delta(\bar{\omega})]}. \tag{28}$$

The detail of calculating the storage modulus and loss modulus that represent the real and imaginary parts of $C^*(\bar{\omega})$ is recorded in the appendix, Eq. (23A), where their formulas for $C'(\bar{\omega})$ and $C''(\bar{\omega})$ are given as

$$C'(\bar{\omega}) = \frac{2}{1-a^2}(m_6 + m_7) \quad \text{and}$$

$$C''(\bar{\omega}) = \frac{2}{1-a^2}(n_6 + n_7), \tag{29}$$

where the coefficients m_6, n_6, m_7, and n_7 are defined as

$$\begin{cases} m_6 = \dfrac{(\beta_1\beta_3 - \beta_2\beta_4)\beta_5 + (\beta_1\beta_4 + \beta_2\beta_3)\beta_6}{\beta_5^2 + \beta_6^2}, \\ n_6 = \dfrac{[(\beta_1\beta_3 - \beta_2\beta_4)\beta_6 + (\beta_1\beta_4 + \beta_2\beta_3)\beta_5]}{\beta_5^2 + \beta_6^2}, \end{cases} \tag{30}$$

with

$$\begin{cases} \beta_1 = \hat{C}_{rz}^d \dfrac{1-a^2}{2} + \left(\dfrac{\hat{A}_r}{\hat{C}_{rr}^d}\hat{C}_{rz}^d - \hat{A}_z\right)\left(am_4 + \dfrac{1-a^2}{2}\right), \\ \beta_2 = a\left(\dfrac{\hat{A}_r}{\hat{C}_{rr}^d}\hat{C}_{rz}^d - \hat{A}_z\right)n_4, \\ \beta_3 = \left[\hat{C}_{rz}^d\left(a^2 - 1\right)K_{rr} - m_5\right], \beta_4 = n_5, \\ \beta_5 = \dfrac{\hat{C}_{r\theta}^d + \hat{C}_{rr}^d}{2}\left(1-a^2\right)K_{rr} + \left(m_2\left(\hat{A}_r - \hat{A}_z\right) - \hat{A}_r\right) \\ \qquad \times \hat{A}_z\Upsilon - m_5, \beta_6 = \left(\hat{A}_r - \hat{A}_z\right)n_2\Upsilon - n_5. \end{cases} \tag{31}$$

and

$$\begin{cases} m_7 = \hat{C}_{zz}^d \dfrac{1-a^2}{2} + \dfrac{\hat{A}_z\Upsilon}{K_{rr}}\left(\dfrac{\hat{C}_{rz}^d}{\hat{C}_{rr}^d} - \dfrac{\hat{A}_z}{\hat{A}_r}\right)\left(am_4 + \dfrac{1-a^2}{2}\right), \\ n_7 = \left(\dfrac{\hat{C}_{rz}^d}{\hat{C}_{rr}^d} - \dfrac{\hat{A}_z}{\hat{A}_r}\right)\dfrac{a\hat{A}_z n_4\Upsilon}{K_{rr}}, \end{cases} \tag{32}$$

where m_1, n_1, m_2, n_2, m_4, n_4, m_5, and n_5 are defined in the appendix A, Eqs. (7A, 8A, 9A, 11A, and 13A) and involve the Kelvin functions ber_n and bei_n ($n = 0, 1$).

4 Numerical results

The loss modulus, storage modulus, and loss tangent are calculated as functions of the permeability, porosity, and frequency for the case of a cylindrical osteon subjected to cyclic loading using Eqs. (28) and (29). For these calculations, two sets of bone elastic constants are needed. The first set is the matrix material constants (E_r^m, E_z^m, $v_{r\theta}^m$, v_{rz}^m, and v_{zr}^m), and the second set is the drained poroelastic constants (E_r^d, E_z^d, $v_{r\theta}^d$, v_{rz}^d, and v_{zr}^d). The values of the matrix material constants are adopted from Cowin et al. (2009) and summarized in Table 3. The drained elastic constants and the drained Poisson's ratios can be approximated as a function of the porosity and the matrix material constants (Yang et al. 1999),
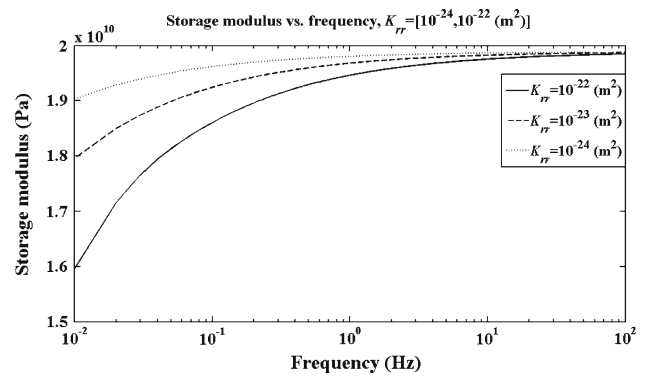
Fig. 3 Plots of the storage modulus $C'(\bar{\omega})$, Eq. (29), as a function of frequency in the PLC, considering 10% porosity (ϕ) and three different values of permeability, $K_{rr} = \{10^{-22},\ 10^{-23},\ 10^{-24}\ (\text{m}^2)\}$
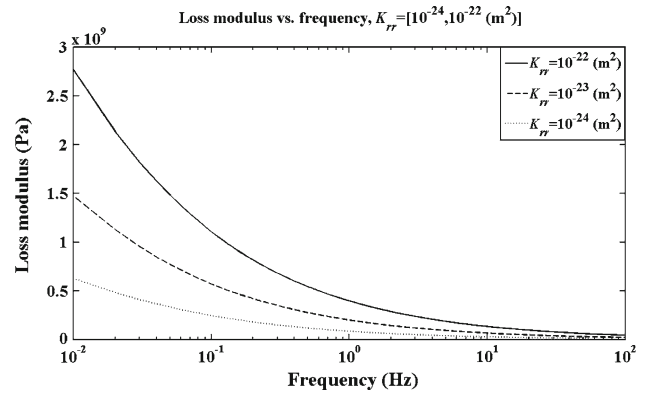
Fig. 4 Plots of the loss modulus $C''(\bar{\omega})$ Eq. (29), as a function of frequency in the PLC, using $\phi = 0.01$ and $K_{rr} = \{10^{-22}, 10^{-23}, 10^{-24}\ (\text{m}^2)\}$ as a function of frequency

$$\begin{aligned} & E_r^d = E_r^m(1-\phi)^{1.92}, \quad E_z^d = E_z^m(1-\phi)^{2.80}, \\ & v_{r\theta}^d = 0.298(1-\phi)^{-0.45}, \quad v_{rz}^d = 0.246(1-\phi)^{-0.19}, \\ & v_{zr}^d = 0.295(1-\phi)^{-0.69}. \end{aligned} \tag{33}$$

The behavior of the storage and loss moduli as functions of frequency in an osteon is shown, respectively, in Figs. 3 and 4. This result was obtained considering 10% porosity (Table 4) and using three different values of intrinsic permeability, 10^{-22}, 10^{-23}, and 10^{-24} m^2 of the PLC. In these two figures, the loss modulus decreases and the storage modulus increases as the permeability decreases from 10^{-22} to 10^{-24} m^2 within the range of frequency analyzed (0.01 to 100 Hz). Therefore, the loss tangent, the ratio of the loss modulus to the storage modulus, should decrease when the permeability decreases, as shown in Fig. 5, the plot of loss tangent.

The storage modulus, the loss modulus, and the loss tangent are larger at low frequencies, respectively, from Figs. 3, 4, and 5; therefore, the calculations of loss tangent shown in Fig. 6 were limited to the frequency range [0.01–1 (Hz)]. Figure 6 is a 3D plot of the loss tangent with respect to porosity and permeability at three different frequencies [0.01, 0.1, 1 (Hz)]. This figure provides the possibility of analyzing the

Table 4 Values of the PLC porosity collected from different studies

Reference	Method	PLC porosity (%)
Gardinier et al. (2010)	Based on Cowin (1999)	5
Fritton, S[a]	Confocal microscopy and microstructural measurements	10
Goulet et al. (2009)	Theoretical estimation based on capillaric and spherical-shell models	12
Ciani et al. (2007)	Scanning electron microscopy	19
Kameo et al. (2010)	Confocal microscopy and microstructural measurements	23

The values are ranging from 5 to 23%

[a] Personnel communication based on on-going study
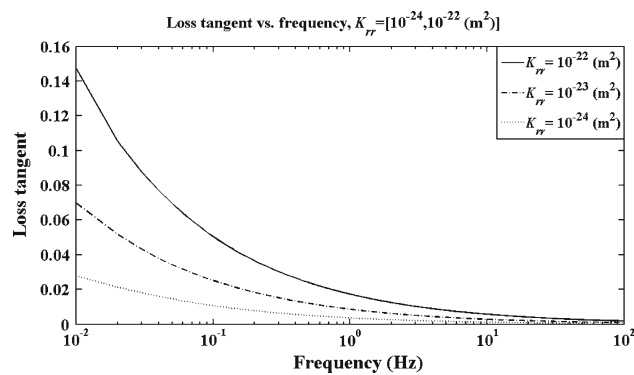
Fig. 5 Plots of the loss tangent $\tan[\delta(\bar{\omega})]$ in the PLC, Eq. (28), using $\phi = 0.01$ and $K_{rr} = \{10^{-22}, 10^{-23}, 10^{-24} \, (\text{m}^2)\}$ versus frequency. The loss tangent is the ratio of the imaginary and real parts of the normalized average resultant stress
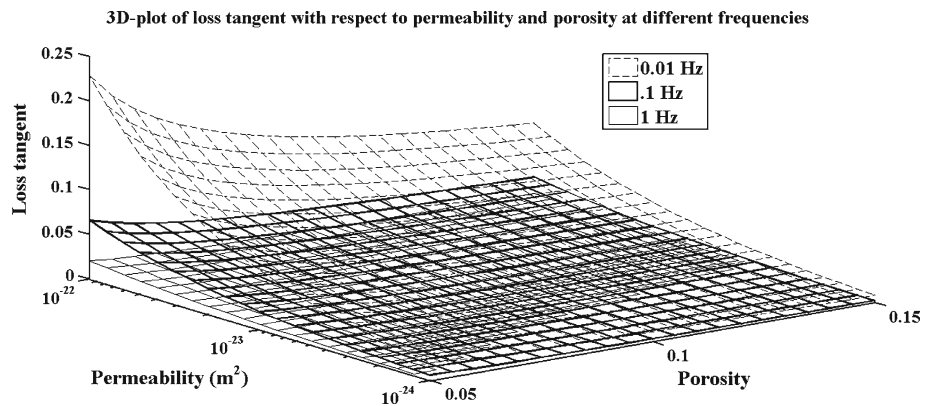
behavior of the loss tangent from three different perspectives. First, it shows how the loss tangent decreases as the frequency increases for different values of porosity and permeability. Second, at any constant value of porosity, it shows that the loss tangent increases with an increase in permeability. Third, it illustrates how the loss tangent decreases when the porosity increases at any constant value of permeability.
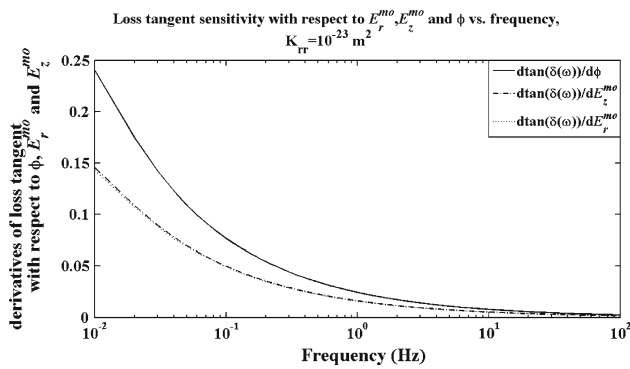
5 Sensitivity of the analytical model

The study of sensitivity of the loss tangent to the variability of the parameters employed in the evaluation of the expression for the loss tangent can be performed in two different ways. The first method is called derivative-based sensitivity analysis (Wu et al. 2011) and consists of determining the partial derivative of the loss tangent with respect to each parameter that may play a key role in determining the value of the expression for the loss tangent. Each partial derivative represents the rate of change of the loss tangent with respect to the related parameter. In other words, the output of each partial derivative illustrates how the corresponding parameter influences the loss tangent, and a plot of all the partial derivatives will depict the hierarchy of the corresponding parameters in terms of their degree of influence on the behavior of the loss tangent. The second method is called numerical parametric sensitivity analysis (Ramtani 2007), and it is based on perturbing the value of each parameter individually with a given percentage of variation considered to be representative of the physiological variability in the osteon. The coefficient of variation, CV, produced in the output of the model (loss tangent) as a consequence of the change in value of an input parameter was calculated as the ratio between the standard deviation SD and the mean value of the loss tangent generated by the variation on each input of the model individually (Eq. 30),

$$CV = 100 \frac{SD\left(\tan[\delta(\bar{\omega})]\right)}{\text{mean}\left(\tan[\delta(\bar{\omega})]\right)}. \tag{34}$$

Fig. 6 3D plots of loss tangent $\tan[\delta(\bar{\omega})]$ with respect to porosity and permeability at three different frequencies, 0.01, 0.1, and 1 (Hz). The ranges of permeability and porosity are, respectively, $[10^{-22}, 10^{-24} \, (\text{m}^2)]$ and $[0.05, 0.15]$

Loss tangent sensitivity with respect to E_r^{mo}, E_z^{mo} and ϕ vs. frequency, $K_{rr} = 10^{-23}$ m^2

Fig. 7 Derivative-based sensitivity plot of the loss tangent with respect to porosity and dimensionless matrix material Young's moduli with $K_{rr} = 10^{-23}$ m^2. The higher curve with the *solid linetype* corresponds to the partial parametric derivative of the loss tangent while the two other curves with the *dotted* and the *dashed linetypes* correspond, respectively, to the partial parametric derivatives of the loss tangent with respect to the normalized elastic matrix material constants E_r^{mo} and E_z^{mo}

The sensitivity of the solution for the loss tangent with respect to its significant parameters other than the permeability, specifically the porosity and the two Young's moduli of the matrix material, the radial E_r^m and the axial E_z^m, was evaluated. The algebraic expressions for the loss tangent and its derivative with respect to porosity are dimensionless while the derivatives of the loss tangent with respect to the elastic material constants are not. In order to plot and compare the partial parametric derivatives of the loss tangent, the derivatives with respect to the Young's moduli are made non-dimensional. The non-dimensionalized radial E_r^m and the axial E_z^m Young's moduli are then given by

$$E_i^{mo} = \frac{E_i^m}{K^f} \quad (i = r, z), \tag{35}$$

where E_i^{mo} are the dimensionless Young's moduli in the radial ($i = r$) and axial ($i = z$) directions while K^f is the compressibility of the interstitial fluid. Figure 7 shows the results of the derivative-based sensitivity analysis by indicating the degree of influence of each parameter on the output of the loss tangent model. The higher curve with the solid linetype corresponds to the partial derivative of the loss tangent with respect to porosity while the two lower curves with the dotted and the dashed linetypes correspond to the derivatives of the loss tangent with respect to the dimensionless matrix material Young's moduli E_r^{mo} and E_z^{mo}. The hierarchy of the three curves shows that the influence of the porosity on the values of the loss tangent is much higher than the influence of the axial or radial matrix material Young's moduli. This behavior was confirmed by using the numerical parametric sensitivity analysis method. A -20% to $+20\%$ perturbation was applied independently to each set of parameters, resulting in an average deviation on the loss tangent of 20% in the case of the porosity while it did not exceed, respectively,

0.8% and 1% for the case of the radial and the axial matrix material Young's moduli.

6 Discussion

This paper is a part of a continuing work aimed at the development of a model describing fluid transport in bone. More specifically, the present study is an extension of previous work (Cowin et al. 2009), which addressed the question of pore fluid movement due to cyclic loading and blood pressure from the perivascular region to the bone cells in the lacunae. The governing equation for the theory of poroelastic material with hierarchical pore structure and compressible constituents in Cowin et al. (2009) was adjusted to fit this case where only the PLC is included and the PV is excluded.

Recently, we have determined the PLC permeability of an isolated osteon using stress-relaxation measurements (Gailani et al. 2009) that were based on a stress-relaxation poroelastic model of an annular poroelastic cylinder as described in Gailani and Cowin (2008). The stress-relaxation test procedure was replaced in this study by cyclic loading, which is closer to the normal physiological loading condition in bones than the stress-relaxation test. Ambulation of a human body involves frequencies of about 1 Hz, and muscles have operational frequencies in the 30 Hz range while measurements have shown that frequencies of several hundred Hertz occur in moving living bones (Cowin and Doty 2007).

The phase angle that an osteonal specimen exhibits under cyclic mechanical loading in the case of specified elastic constants depends mainly upon the permeability and porosity. Expressions for the storage modulus, loss modulus, and loss tangent are obtained from the poroelastic model. Figures 3, 4, and 5 depict, respectively, the 2D plots of the storage modulus, the loss modulus, and the loss tangent with respect to frequency for the parameter values specified in Table 3. Figure 6 illustrates the 3D plots of the loss tangent with respect to permeability and porosity at different frequencies [0.01, 0.1, 1 (Hz)] while Fig. 7 represents the plots of the loss tangent derivatives with respect to the porosity and the elastic matrix material Young's moduli at a permeability of 10^{-23} m^2. The plots in Fig. 3 refer to the storage modulus, which illustrate how the effective stiffness of an osteon specimen behaves with frequency. At low frequencies, these curves increase sharply; then, the increasing rate of the storage modulus starts decreasing monotonically until it becomes almost steady around 10^2 Hz. The plots of Fig. 4 represent the loss modulus while Figs. 5 and 6 represent the loss tangent. The plots of loss tangent and loss modulus express how the energy dissipation and mechanical damping vary in an osteonal sample with respect to frequency, permeability, and porosity. In contrast to the curves for the storage modulus that are increasing with frequency, the curves

for the loss modulus (Fig. 4) and the loss tangent (Fig. 5) are decreasing. At high frequencies, these curves converge toward zero asymptotically, which means that the behavior of the bone sample at high frequencies is purely elastic. The storage modulus, the loss modulus, and the loss tangent are, respectively, represented with cosine, sine, and tangent of the phase angle by the formulas represented in Eqs. (27) and (28). In other words, this means that there is a causal relation between the variability of these physical properties and the variation of the phase angle. The results from this analytical model are the foundation for the experimental design of a forthcoming study, in which the variation of the phase angle with respect to frequency will be used to determine the permeability of the lacunar–canalicular porosity in a section of a single osteon. In particular, it can be inferred from the curves in Figs. 3, 4, 5, and 7 that the most sensitive range of frequency for the planned experimental study would be between 10^{-2} and 10^1 Hz. Importantly, this range of frequency contains the physiological level of frequency at which mechanical loading is considered to be applied to bone in humans. Moreover, it can be concluded from Fig. 7 that the porosity is the most influential parameter affecting the magnitude of the loss tangent, and that the loss tangent is highly sensitive to the frequency, decreasing exponentially as the frequency increases.

The numerical results produced by our model are close to the results of loss tangent previously reported in the literature. For instance, the values of loss tangent predicted by this model and presented in Fig. 5 are close to the experimental loss tangent curves presented by Garner et al. (2000). From their Figs. 5 and 4, the reported values of loss tangent are between 0.06 at 10^{-2} Hz and 0.02 at 10^2 Hz. In another study by Drabousky (2009), the loss modulus and storage modulus are plotted in their figures 3.20 and 3.22, respectively. At the same frequencies, the values of loss tangent calculated from their curves vary from 0.075 to 0.015. In this study, the values of the loss tangent obtained from our analytical model are between 0.14 at 10^{-2} Hz and 0.005 at 10^2 Hz. The small differences in the behavior of the storage modulus, the loss modulus, and the loss tangent that can be observed with a comparison of the plots in Figs. 3, 4, and 5 with the corresponding figures from Garner et al. (2000) and Drabousky (2009) may be attributed to two facts. First, we assumed that our specimens were microscopic cylindrical sections of osteons that included only the PLC and excluded the PV, while they used in both studies macroscopic samples that included the PLC and the PV. Second, we calculated our analytical models based on cyclic strain and resultant stresses, while in both papers, they adopted different experimental approaches to determine their data. In Garner et al. (2000), the loss tangent was determined in cylindrical specimen harvested from human tibia in the transversal and longitudinal directions. For the transversal direction, the authors used bending moments and resultant bending deformation while in the longitudinal direction, they used harmonic torque and resultant angular displacement experiments. Concerning the second paper, Drabousky (2009) used tensile relaxation tests at different load magnitudes and strain rates to determine the loss modulus and the storage modulus in cylindrical equine cortical bone specimens.

Finally, the present work contains two limitations. First, the geometrical idealization of the osteonal specimen as a right circular cylinder approximately corresponds to the shape of the osteon. Second, the impermeable boundary condition assumed at the cement line for the ODE (4) might not be totally correct. Wang et al. (1999) assumed that the cement line is slightly permeable. However, even if this permeability exists, it is negligible in comparison to the one at the inner boundary between the PLC and the PV porosities.

Appendix: Determination of the real and imaginary parts of $C^*(\bar{\omega})$

The expression of the modulus $C^*(\bar{\omega})$ in Eq. (22) contains hierarchical complex components such as a_1 and $\frac{a\bar{\Sigma}(a,1)}{\sqrt{i\bar{\omega}}}$ with

$$\bar{\Sigma}(a,1) = \frac{\Sigma(a,1)}{\Pi(a,1)}, \tag{1A}$$

and

$$\begin{cases} \Sigma(a,1) = I_1(a\sqrt{i\bar{\omega}})K_1\left(\sqrt{i\bar{\omega}}\right) - I_1\left(\sqrt{i\bar{\omega}}\right)K_1\left(a\sqrt{i\bar{\omega}}\right), \\ \Pi(a,1) = I_o\left(a\sqrt{i\bar{\omega}}\right)K_1\left(\sqrt{i\bar{\omega}}\right) + I_1\left(\sqrt{i\bar{\omega}}\right)K_o\left(a\sqrt{i\bar{\omega}}\right) \end{cases} \tag{2A}$$

where I_n and K_n ($n = 0, 1$) are Bessel functions. Now if we let $x_1 = \sqrt{\bar{\omega}}$ and $x_2 = a\sqrt{\bar{\omega}}$, the forms of $\Sigma(a,1)$ and $\Pi(a,1)$ in (2A) are rewritten as

$$\begin{cases} \Pi(a,1) = I_o\left(x_2\sqrt{i}\right)K_1\left(x_1\sqrt{i}\right) + I_1\left(x_1\sqrt{i}\right)K_o\left(x_2\sqrt{i}\right), \\ \Sigma(a,1) = I_1\left(x_2\sqrt{i}\right)K_1\left(x_1\sqrt{i}\right) - I_1\left(x_1\sqrt{i}\right)K_1\left(x_2\sqrt{i}\right). \end{cases} \tag{3A}$$

From Abramowitz and Stegun (1964, equations (9.9.1) and (9.9.2)), we have

$$\begin{cases} I_o\left(xe^{\frac{i\pi}{4}}\right) = ber_o x + i(bei_o x), \quad I_1\left(xe^{\frac{i\pi}{4}}\right) = bei_1 x - i(ber_1 x), \\ K_o\left(xe^{\frac{i\pi}{4}}\right) = ker_o x + i(kei_o x), \quad K_1\left(xe^{\frac{i\pi}{4}}\right) = -kei_o x + i(ker_o x), \end{cases} \tag{4A}$$

where ber_n, bei_n ($n = 0, 1$) are Kelvin functions. Thus,

$$I_o\left(x_2\sqrt{i}\right)K_1\left(x_1\sqrt{i}\right)$$
$$= [ber_o x_2 + i(bei_o x_2)][-kei_1 x + i(ker_1 x)]$$
$$= -ber_o x_2 kei_1 x_1 + i(ber_o x_2\, ker_1\, x_1)$$
$$\quad -i(bei_o x_2 kei_1 x_1) - bei_o x_2 ker_1 x_1$$
$$= -ber_o x_2 kei_1 x_1 - bei_o x_2 ker_1 x_1$$
$$\quad +i(ber_o x_2 ker_{11} x_1 - bei_o x_2 kei_1 x_1), \tag{5A}$$

and

$$I_1\left(x_1\sqrt{i}\right)K_o\left(x_2\sqrt{i}\right)$$
$$= [bei_1 x_1 - i(ber_1 x_1)][ker_o x_2 + i(kei_o x_2)]$$
$$= bei_1 x_1 ker_o x_2 + i(bei_1 x_1 kei_o x_2)$$
$$\quad -i(ber_1 x_1 ker_o x_2) + ber_1 x_1 kei_o x_2$$
$$= bei_1 x_1 ker_o x_2 + ber_1 x_1 kei_o x_2$$
$$\quad +i(bei_1 x_1 kei_o x_2 - ber_1 x_1 ker_o x_2), \tag{6A}$$

which means

$$\Pi(a, 1)$$
$$= I_o\left(x_2\sqrt{i}\right)K_1\left(x_1\sqrt{i}\right) + I_1\left(x_1\sqrt{i}\right)K_o\left(x_2\sqrt{i}\right)\Big]$$
$$= -ber_o x_2 kei_1 x_1 - bei_o x_2 ker_1 x_1$$
$$\quad +i(ber_o x_2 ker_1 x_1 - bei_o x_2 kei_1 x_1)$$
$$\quad +bei_1 x_1 ker_o x_2 + ber_1 x_1 kei_o x_2$$
$$\quad +i(bei_1 x_1 kei_o x_2 - ber_1 x_1 ker_o x_2)$$
$$= -ber_o x_2 kei_1 x_1 - bei_o x_2 ker_1 x_1 + bei_1 x_1 ker_o x_2$$
$$\quad +ber_1 x_1 kei_o x_2 + i(ber_o x_2 ker_1 x_1 - bei_o x_2 kei_1 x_1$$
$$\quad +bei_1 x_1 kei_o x_2 - ber_1 x_1 ker_o x_2).$$
$$= m_1 + in_1. \tag{7A}$$

Following the expression (7A) the term $\frac{1}{\sqrt{i\bar\omega}\Pi(a,1)}$ in Eq. (8) is rewritten as

$$\frac{1}{\sqrt{i\bar\omega}\Pi(a,1)} = \frac{1}{\sqrt{i\bar\omega}(m_1 + in_1)} = m_2 + in_2 \text{ since}$$
$$\sqrt{i\bar\omega} = \sqrt{\bar\omega}e^{\frac{i\pi}{4}} = \sqrt{\frac{\bar\omega}{2}}(1 + i) \tag{8A}$$

with

$$m_2 = \frac{m_1 - n_1}{\sqrt{\frac{\bar\omega}{2}((m_1 - n_1)^2 + (m_1 + n_1)^2)}} \text{ and}$$
$$n_2 = \frac{-m_1 - n_1}{\sqrt{\frac{\bar\omega}{2}\left((m_1 - n_1)^2 + (m_1 + n_1)^2\right)}}. \tag{9A}$$

From the other side the substitution of Eqs. (4A) into the form of $\Sigma(a, 1)$ from (3A) leads to

$$\Sigma(a, 1)$$
$$= I_1\left(x_2\sqrt{i}\right)K_1\left(x_1\sqrt{i}\right) - I_1\left(x_1\sqrt{i}\right)K_1\left(x_2\sqrt{i}\right)$$
$$= -ber_1 x_2 kei_1 x_1 - bei_1 x_2 ker_1 x_1$$
$$\quad +i(ber_1 x_2 ker_1 x_1 - bei_1 x_2 kei_1 x_1)$$
$$\quad -bei_1 x_1 ker_1 x_2 - ber_1 x_1 kei_1 x_2$$
$$\quad -i(-bei_1 x_1 kei_1 x_2 + ber_1 x_1 ker_1 x_2)$$
$$= -ber_1 x_2 kei_1 x_1 - bei_1 x_2 ker_1 x_1 - bei_1 x_1 ker_1 x_2$$
$$\quad -ber_1 x_1 kei_1 x_2$$
$$\quad +i(ber_1 x_2 ker_1 x_1 - bei_1 x_2 kei_1 x_1 - bei_1 x_1 kei_1 x_2$$
$$\quad +ber_1 x_1 ker_1 x_2)$$
$$= m_3 + in_3, \tag{10A}$$

and by replacing (8A) and (10A) in $\frac{\bar\Sigma(a,1)}{\sqrt{i\bar\omega}}$ defined in Eqs. (1A) and (8A), the general form becomes

$$\frac{\bar\Sigma(a, 1)}{\sqrt{i\bar\omega}} = m_4 + in_4, \tag{11A}$$

where

$$\begin{cases} m_4 = \sqrt{\frac{2}{\bar\omega}}\frac{m_3(m_1+n_1)+n_3(n_1-m_1)}{m_1^2+n_1^2}, \\ n_4 = \sqrt{\frac{2}{\bar\omega}}\frac{m_3(m_1-n_1)+n_3(n_1+m_1)}{m_1^2+n_1^2}. \end{cases} \tag{12A}$$

Then, by substituting Eqs. (11A) and (8A) into Eq. (17) the expression of a_1 is rewritten as

$$a_1 = m_5 + in_5, \tag{13A}$$

where

$$\begin{cases} m_5 = \frac{\left(\hat{C}_{rr}^d - \hat{C}_{r\theta}^d\right)}{\hat{C}_{rr}^d}\left(am_4 + \frac{1-a^2}{2} - m_2\right)\hat{A}_z\Upsilon, \\ n_5 = \left(a\frac{\left(\hat{C}_{rr}^d - \hat{C}_{r\theta}^d\right)}{\hat{C}_{rr}^d}n_4 - n_2\right)\hat{A}_z\Upsilon. \end{cases} \tag{14A}$$

Now let's write $C^*(\bar\omega)$ from Eq. (22) as

$$C^*(\bar\omega) = \frac{2}{1-a^2}[H_1 + H_2], \tag{15A}$$

where

$$H_1 = \left[\hat{C}_{rz}^d\frac{1-a^2}{2} - \left(\frac{\hat{A}_r}{\hat{C}_{rr}^d}\hat{C}_{rz}^d - \hat{A}_z\right)\left(\frac{a\bar\Sigma(a, 1)}{\sqrt{i\bar\omega}} + \frac{1-a^2}{2}\right)\right]$$
$$\times \frac{\left[a_1 - \hat{C}_{rz}^d\left(1-a^2\right)K_{rr}\right]\varepsilon_o}{\frac{\hat{C}_{r\theta}^d+\hat{C}_{rr}^d}{2}\left(1-a^2\right)K_{rr} + \left(\frac{\hat{A}_r-\hat{A}_z}{\sqrt{i\bar\omega}\Pi(a,1)} - \hat{A}_r\right)\hat{A}_z - a_1}, \tag{16A}$$

and

$$H_2 = \hat{C}_{zz}^d\frac{1-a^2}{2} + \left(\frac{\hat{C}_{rz}^d}{\hat{C}_{rr}^d} - \frac{\hat{A}_z}{\hat{A}_r}\right)$$
$$\times \left(\frac{a\bar\Sigma(a, 1)}{\sqrt{i\bar\omega}} + \frac{1-a^2}{2}\right)\frac{\hat{A}_z\Upsilon}{K_{rr}}. \tag{17A}$$

Thus, from one side the substitution of Eqs. (11A) and (13A) into Eq. (16A) gives

$$
H_1 = \left[\hat{C}_{rz}^d \frac{1-a^2}{2} + \left(\frac{\hat{A}_r}{\hat{C}_{rr}^d} \hat{C}_{rz}^d - \hat{A}_z \right) \left(a(m_4 + in_4) + \frac{1-a^2}{2} \right) \right]
$$

$$
\times \frac{\left\{ \left[m_5 + in_5 - \hat{C}_{rz}^d(a^2 - 1)K_{rr} \right\} \right.}{\frac{\hat{C}_{r\theta}^d + \hat{C}_{rr}^d}{2}(1-a^2)K_{rr} + \left[(m_2 + in_2)(\hat{A}_r - \hat{A}_z) - \hat{A}_r \right] \Upsilon - m_5 - in_5 \right]}
$$

$$
= m_6 + in_6, \tag{18A}
$$

where

$$
\begin{cases}
m_7 = \dfrac{(\beta_1\beta_3 - \beta_2\beta_4)\beta_5 + (\beta_1\beta_4 + \beta_2\beta_3)\beta_6}{\beta_5^2 + \beta_6^2}, \\[2mm]
n_7 = \dfrac{(\beta_1\beta_4 + \beta_2\beta_3)\beta_5 + (\beta_2\beta_4 - \beta_1\beta_3)\beta_6}{\beta_5^2 + \beta_6^2},
\end{cases} \tag{19A}
$$

with

$$
\begin{cases}
\beta_1 = \hat{C}_{rz}^d \frac{1-a^2}{2} + \left(\frac{\hat{A}_r}{\hat{C}_{rr}^d} \hat{C}_{rz}^d - \hat{A}_z \right) \left(am_4 + \frac{1-a^2}{2} \right), \\[2mm]
\beta_2 = a \left(\frac{\hat{A}_r}{\hat{C}_{rr}^d} \hat{C}_{rz}^d - \hat{A}_z \right) n_4, \\[2mm]
\beta_3 = \left[\hat{C}_{rz}^d (a^2 - 1) K_{rr} - m_5 \right], \ \beta_4 = n_5, \\[2mm]
\beta_5 = \frac{\hat{C}_{r\theta}^d + \hat{C}_{rr}^d}{2} (1 - a^2) K_{rr} + \left(m_2 \left(\hat{A}_r - \hat{A}_z \right) - \hat{A}_r \right) \\[2mm]
\quad \times \hat{A}_z \Upsilon - m_5, \quad \beta_6 = \left(\hat{A}_r - \hat{A}_z \right) n_2 \Upsilon - n_5.
\end{cases} \tag{20A}
$$

From the other side, by substituting Eq. (11A) into Eq. (17A), the expression of H_2 is rewritten as

$$
H_2 = m_7 + in_7, \tag{21A}
$$

where

$$
\begin{cases}
m_7 = \hat{C}_{zz}^d \frac{1-a^2}{2} + \frac{\hat{A}_z \Upsilon}{K_{rr}} \left(\frac{\hat{C}_{rz}^d}{\hat{C}_{rr}^d} - \frac{\hat{A}_z}{\hat{A}_r} \right) \left(am_4 + \frac{1-a^2}{2} \right), \\[2mm]
n_7 = \left(\frac{\hat{C}_{rz}^d}{\hat{C}_{rr}^d} - \frac{\hat{A}_z}{\hat{A}_r} \right) \frac{a \hat{A}_z n_4 \Upsilon}{K_{rr}},
\end{cases} \tag{22A}
$$

Finally by introducing Eqs. (23) and (18A) into Eq. (15A) the expression of the normalized pressure $C^*(\bar{\omega})$ is rewritten as

$$
C^*(\bar{\omega}) = C'(\bar{\omega}) + i C''(\bar{\omega}), \tag{23A}
$$

where

$$
\begin{cases}
C'(\bar{\omega}) = \frac{2}{1-a^2}(m_6 + m_7), \\[2mm]
C''(\bar{\omega}) = \frac{2}{1-a^2}(n_6 + n_7).
\end{cases} \tag{24A}
$$

References

Abramowitz M, Stegun IA (1964) Handbook of mathematical functions with formulas, graphs and mathematical tables. Natl Bureau Standards Appl Math Ser 55:379–380

Beno T, Yoon YJ, Cowin SC, Fritton SP (2006) Estimation of bone permeability using accurate microstructural measurements. J Biomech 39:2378–2387

Buechner PM, Lakes RS (2003) Size effects in the elasticity and viscoelasticity of bone. Biomech Model Mechanobiol 1:295–301

Burger EH, Klein-Nulend J, van der Plas A, Nijweide PJ (1995) Function of osteocytes in bone—their role in mechanotransduction. J Nutr 125(7 Suppl):2020S–2023S

Ciani C, Ramirez Marin PAR, Doty SB, Fritton SP (2007) Bone microstructure in OVX and normal rat bone as revealed by confocal and electron microscopy. In: Bioengineering conference, 2007. NEBC '07. IEEE 33rd annual Northeast, pp 23–24

Cowin SC (1999) Bone poroelasticity. J Biomech 32:217–238

Cowin SC (2001) Bone Mechanics Handbook, vol 17, 2nd edn. CRS Press, Boca Raton 2–5

Cowin SC, Doty SB (2007) Tissue mechanics. Springer, Berlin

Cowin SC, Gailani G, Benalla M (2009) Hierarchical poroelasticity: movement of interstitial fluid between porosity levels in bones. Philos Trans R Soc 367:3401–3443

Cowin SC, Moss-Salentijn L, Moss ML (1991) Candidates for the mechanosensory system in bone. J Biomech Eng 113:191–197

Cowin SC, Weinbaum S, Zeng Y (1995) A case for bone canaliculi as the anatomical site of strain-generated potentials. J Biomech 28:1281–1296

Drabousky DP (2009) Prony series representation and interconversion of viscoelastic material functions of equine cortical bone. Department of Mechanical and Aerospace Engineering, Western Reserve University, Cleveland

Fornells P, García-Aznar JM, Doblaré M (2007) A finite element dual porosity approach to model deformation-induced fluid flow in cortical bone. Ann Biomed Eng 35:1687–1698

Fritton SP, Wang L, Weinbaum S, Cowin SC (2001) Interaction of mechanical loading, blood flow, and interstitial fluid flow in osteonal bone. Proc Bioeng Conf BED 50:341–342

Fritton SP, Weinbaum S (2009) Fluid and solute transport in bone: flow induced mechanotransduction. Annu Rev Fluid Mech 41:347–374

Gailani GB, Benalla M, Mahamud R, Cowin SC, Cardoso L (2009) Experimental determination of the permeability in the lacunar-canalicular porosity of bone. J Biomech Eng 131: 1010071–1010077

Gailani GB, Cowin SC (2008) The unconfined compression of a poroelastic annular cylindrical disk. Mech Mater 40:507–523

Gardinier JD, Townend CW, Jen KP, Wu Q, Duncan RL, Wang L (2010) In situ permeability measurement of the mammalian lacunar-canalicular system. J Bone 46:1075–1081

Garner E, Lakes R, Lee T, Swan C, Brand R (2000) Viscoelastic dissipation in compact bone: implications for stress-Induced fluid flow in bone. J Biomech Eng 122:167–172

Goulet GC, Coombe D, Martinuzzi RJ, Zernicke RF (2009) Poroelastic evaluation of fluid movement through the lacunocanalicular system. Ann Biomed Eng 37(7):1390–1402

Gururaja S, Kim HJ, Swan CC, Brand RA, Lakes RS (2005) Modeling deformation-induced fluid flow in cortical bone's canalicular-lacunar system. Ann Biomed Eng 33:7–25

Han Y, Cowin SC, Schaffler MB, Weinbaum S (2004) Mechanotransduction and strain amplification in osteocyte cell processes and flow across the endothelial glycocalyx. Proc Natl Acad Sci USA 101:16689–16694

Jee W (1988) The skeletal tissues. In: Weiss L. (ed) Cell and tissue biology: a textbook of histology. Urban & Schwarzenberg, Baltimore p 207

Kameo Y, Adachi T, Sato N, Hojo M (2010) Estimation of bone permeability considering the morphology of lacuno-canalicular porosity. J Mech Behav Biomed Mater 3:240–248

Lakes RS (1982) Dynamical study of couple stress effects in human compact bone. J Biomech Eng 104:7–11

Nguyen V, Lemaire T, Naili S (2009) Numerical study of deformation-induced fluid flows in periodic osteonal matrix under harmonic axial loading. C R Mecanique 337:268–276

Oyen ML (2008) Poroelastic nanoindentation responses of hydrated bone. J Mater Res 23:1307–1314

Ramtani S (2007) Parametric sensitivity analysis applied to a specific one-dimensional internal bone remodeling problem. Comput Biol Med 37:1203–1209

Rémond A, Naïli S, Lemaire T (2008) Interstitial fluid flow in the osteon with spatial gradients of mechanical properties: a finite element study. Biomech Model Mechanobiol 7:487–495

Smit TH, Huyghe JM, Cowin SC (2002) Estimation of the poroelastic parameters of bone. J Biomech 35:829–836

Swan CC, Lakes RS, Brand RA, Stewart KJ (2003) Micromechanically based poroelastic modeling of fluid flow in Haversian bone. J Biomech Eng 125:25–37

Wang L, Fritton SP, Cowin SC, Weinbaum S (1999) Fluid pressure relaxation depends upon osteonal microstructure: modeling an oscillatory bending experiment. J Biomech 32:663–672

Wang L, Fritton SP, Weinbaum S, Cowin SC (2003) On bone adaptation due to venous stasis. J Biomech 36:1439–1451

Weinbaum S, Cowin SC, Zeng Y (1994) A model for the excitation of osteocytes by mechanical loading-induced bone fluid shear stresses. J Biomech 27:339–360

Wu D, Ci S, Luo H (2011) A theoretical framework for interaction measure and sensitivity analysis in cross-layer design. ACM Trans Model Comput Simulat 21:1–26

Yang G, Kabel J, Rietbergen BV, Odgaard A, Huiskes R, Cowin SC (1999) The anisotropic Hooke's law for cancellous bone and wood. J Elast 53:125–146

Zeng Y, Cowin SC, Weinbaum S (1994) A fiber matrix model for fluid flow and streaming potentials in the canaliculi of an osteon. Ann Biomed Eng 22:280–292

Zhang D, Weinbaum S, Cowin SC (1998) Estimates of the peak pressures in the bone pore water. J Biomech Eng 120:697–703

Zhou X, Novotny JE, Wang L (2008) Modeling fluorescence recovery after photobleaching in loaded bone: potential applications in measuring fluid and solute transport in the osteocytic lacunar-canalicular system. Ann Biomed Eng 36:1961–1977